Impact of Ho³⁺ Substitution on Structural, Morphological, Optical, Electrical, Thermoelectrical and Magnetic Properties of MgCuHoₓFe₂₋ₓO₄ (0 < x < 0.030) System

M. Bhanu[1,](ORCID), D. Ravinder[1,](ORCID), Police Vishnuvardhan Reddy[2,](ORCID),
K. Rajashekhar[3,](ORCID), G. Sunitha[4,](ORCID), G. Kumar[4,](ORCID), J. Laxman Naik[1,*,](ORCID) and G. Vinod[4,*,](ORCID)

[1]Department of Physics, Osmania University, Hyderabad-500007, India
[2]Department of Humanities & Science (Chemistry), CVR College of Engineering, Hyderabad-501510, India
[3]Department of Physics, Kamala Institute of Technology and Science, Huzurabad-505468, India
[4]Department of Humanities & Science (Physics), Teegala Krishna Reddy College of Engineering & Technology, Hyderabad-500097, India

*Corresponding authors: E-mail: laxmannaikj@gmail.com; vinodg3232@gmail.com

A series of rare earth (Ho³⁺) doped magnesium-copper nanoferrites with the general chemical compositions of $Mg_{0.5}Cu_{0.5}Ho_xFe_{2-x}O_4$ (where x = 0.000, 0.005, 0.010, 0.015, 0.020, 0.025 and 0.030) was fabricated by citrate sol-gel auto-combustion technique. The fabricated materials were investigated through powder XRD, FESEM, EDX, HRTEM, FTIR, UV-Vis, DC resistivity, TEP and VSM for magnetic properties. The crystallite size of the samples was determined to be in the range of 33-40 nm with increased Ho³⁺ content and the powder-XRD investigations validated the spinel cubic structure of the samples with the space group $Fd\bar{3}m$. The analysis demonstrated that the lattice constant was reduced from 8.403 to 8.356 Å and according to the FE-SEM micrographs, the morphology of the samples were found to be spherical. The HR-TEM micrographs show that average particle size decreases from 64 to 48 nm. The FTIR examination revealed that their ν_1 and ν_2 absorption bands were located between 412-401 cm⁻¹ and 562-547 cm⁻¹, respectively and the optical band gap was found to be 2.77-3.28 eV. In Mg-Cu nanoferrites with Ho doping, there was no obvious increase in the elasticity moduli. It was observed that the thermal energy required to transform the p-type Mg-Cu nanoferrites from semiconducting to n-type semiconducting behaviour increases with increasing Ho doping and composition. The M-H loop saturation magnetization (M_s), coercivity (H_c) and retentivity (M_r) values were all enhanced when the Ho³⁺ concentration increased and varied anisotropically with Ho doping. The findings of this study suggested that Mg-Cu ferrites doped with Ho³⁺ might be beneficial for magnetic resonance imaging in biomedicine.

Keywords: Ho doping, Mg-Cu nanoferrite, Electrical and Magnetic properties.

INTRODUCTION

Currently, a wide range of magnetic materials with enhanced ferromagnetic materials are produced using various nanocrystalline combinations. Owing to their unique structural, optical and magnetic characteristics, ferrites with spinel structures are significant in their own right [1-3]. There are several approaches to fine-tune these characteristics, such as doping an approved component, depending on the desired application and characterization method. The exceptional electrical and magnetic characteristics of cobalt ferrites make them a material of importance. Spinel ferrites' tetrahedral (A) and octahedral (B) sites' cations and their distribution are essential for these features. Ferrites exhibit ferrimagnetic properties due to a phenomenon known as super-exchange, where an interaction occurs between the oxygen ions and the magnetic moments of materials. These insulating ferrites have high electric resistance, low dielectric loss, low eddy current losses and high permeability. Ferrites exhibit diverse magnetic properties based on their composition and preparation methods [4-6].

The spinel nanoferrites are produced *via* a sol-gel process or precursor autocombustion, coprecipitation, hydrothermal, microwave combustion and co-precipitation [7-10]. The citrate precursor method offers several benefits, including uniform atomic level mixing of the cations, a constrained size distribution, exact stoichiometry control, cost-effectiveness and low-temperature phase formation [11-13]. Cation distribution has a significant role in controlling the magnetization of spinel nano-

ferrite, which is proportional to the magnetization differential (M_B-M_A) between the B and A sub-lattices. Single-ion aniso-tropy of Co^{2+}, Fe^{3+} and Fe^{2+} depends on the occupancy site [14-18]. The cation distribution affects magnetic anisotropy, correlated coercivity and surface canting. Several publications have characterized Mg-Cu nanoferrites as magnetic materials with good transitions in their magnetization. This flexibility results from copper ferrite, depending on the inversion para-meter, being either an antiferromagnetic or ferromagnetic material, while copper ferrite is ferrimagnetic [19-22].

Applications for the thermal heating of an integrated nano-ferrite used in cancer treatment depend on several variables, including safe compositions, small molecular weights, small particle sizes, appropriate saturation magnetization and low coercivity. To enhance the magnetic and elastic properties of spinel ferrites, several authors have looked into the substitution of magnetic Fe^{3+} cation with nanomagnetic ones such as Sm^{3+} and Cr^{3+} at various substitution levels [23-27]. In this study, it has been observed that both the structural and magnetic charac-teristics exhibit non-monotonic behaviour when the substitution level increases. Those findings were discussed in the proposed sample and compared to the experimental findings from power XRD, FESEM, HRTEM, FTIR, UV-vis and VSM techniques. In present work, holonium doped magnesium and copper nano-ferrites were prepared *via* the citrate sol-gel auto-combustion method. The impact of Ho^{3+} ions on the structural, optical, morp-hological and magnetic properties of magnesium and copper nanoferrites $Mg_{0.5}Cu_{0.5}Ho_xFe_{2-x}O_4$ (with x = 0.00-0.030) was also studied.

EXPERIMENTAL

Synthesis procedure: The citrate sol-gel auto-combustion technique has been used to synthesize Ho-doped Mg-Cu ferrites, which were prepared from magnesium nitrate hexahydrate $(Mg(NO_3)_2 \cdot 6H_2O)$, copper nitrate hexahydrate $(Cu(NO_3)_2 \cdot 6H_2O)$, ferric nitrate hexahydrate $(Fe(NO_3)_3 \cdot 9H_2O)$ and holonium nitrate hexahydrate $(Ho(NO_3)_3 \cdot 6H_2O)$. To produce a homogeneous solution, the raw compounds were separately dissolved in 80 mL of deionized water at a precise stoichiometric ratio. The subsequent stage involved dissolving the precursors into a beaker and stirred for 45 min using a magnetic stirrer. The homo-geneous solution was mixed with citric acid while using the magnetic stirrer at 70 ℃. Added ammonia solution to the above mixture dropwise to maintain pH 7. The mixture was subsequently heated on a magnetic stirrer hot plate with continuous stirring until it reached a dry state, resulting in the formation of a gel. The resulting materials were calcined in a furnace at 70 ℃ for 5 h to obtain the spinel phase.

Characterization: The powder XRD analysis of the samples were conducted on the Rigaku Miniflex-600, Japan with radiation (λ = 1.5406 Å). The FESEM (Oxford Instrument Inca X-act) analysis was employed to determine grain size and morphology. The HRTEM technique (HRTEM, JEM-F200 Multi-purpose electron microscope) was used to examine the cross-sections and particle size of the nanoferrites. The FTIR spectro-scopy uses confirmed the absorption bands (v_1, v_2). A UV-vis spectrometer (Perkin) was used to investigate the optical band

gap. The Lake Shore Cryotronics 8600 Series instrument, based on the Vector Space Model (VSM), was utilized to investigate the temperature-dependent magnetic properties and M-H hyst-eresis loops of Ho doped magnesium and copper nanoferrites. The two-probe method was employed for this purpose, along with measurements of the DC electrical system. To investigate the connection between thermoelectric power, temperature and composition, the differential technique was adopted.

RESULTS AND DISCUSSION

Powder XRD studies: Fig. 1 demonstrates the powder X-ray diffraction of Ho substituted Mg-Cu nanospinel ferrite within 10-80º 2θ at room temperatures. The XRD technique was employed to determine the crystal structure and identified the crystalline phase. The miller peaks with the following indices *viz.* (111), (220), (311), (222), (400), (422), (511), (440) and (533) were identified which are closely matched with the Mg-Cu ferrite peaks and belong to JCPD card no. #00-001-1109. It was evident from the P-XRD pattern that Ho^{3+} ions were appropriately doped into the prepared nanoferrite samples since no additional peaks in the Ho-doped magnesium-copper nanoferrite samples were obtained. The average crystallite size of the prepared samples was calculated using the Debye-Scherrer's formula from the center peak (311) plane [28,29].

$$D_{P-XRD} (nm) = \frac{k\lambda}{\beta\cos\theta} \quad (1)$$

where D_{P-XRD} stands for crystallite size, constant 0.9 is the correction factor for sphere-shaped particles, λ = 1.5406 Å is the wavelength of the Cu-target and indicates full-width half maximum (FWHM) and θ is the Bragg's angle of the peak with the highest intensity. Table-1 summarizes the computed crystallite size values (D_{P-XRD}). By increasing dopant Ho^{3+} content (x = 0.00-0.030), the average crystallite size of the generated samples was decreased from 32.03 nm to 20.20 nm. The miller indices (*hkl*) and interplanar spacing (d) data were used to derive the lattice parameter (a) as:

$$a (\text{Å}) = d\sqrt{h^2 + k^2 + l^2} \quad (2)$$

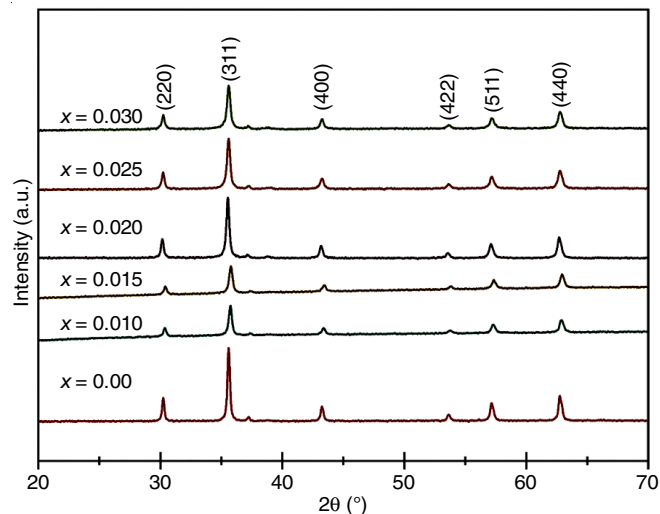Fig. 1. X-ray diffraction patterns of $Mg_{0.5}Cu_{0.5}Ho_xFe_{2-x}O_4$ nanoferrite

TABLE-1
Ho^{3+} CONCENTRATION (x), CRYSTALLITE SIZE (nm), LATTICE CONSTANT (a), CELL VOLUME X-RAY DENSITY (d$_x$), BULK DENSITY (d$_B$), POROSITY (P) PERCENTAGE AND TETRAHEDRAL (A-) SITE HOPPING LENGTH 'L$_A$' AND OCTAHEDRAL (B-) SITE HOPPING LENGTH 'L$_B$' FOR Mg$_{0.5}$Cu$_{0.5}$Ho$_x$Fe$_{2-x}$O$_4$ NANOFERRITES

Samples (x)	Crystallite size (nm)	Lattice constant (Å)	Cell volume (Å^3)	X-ray density (g/cm^3)	Bulk density (g/cm^3)	Porosity (ρ%)	L$_A$ (Å)	L$_B$ (Å)
0.000	32.03	8.395	589.592	4.948	2.732	48.78	3.630	2.964
0.010	22.55	8.331	591.6462	5.131	3.202	50.12	3.609	2.943
0.015	17.10	8.348	578.2177	5.143	3.410	52.11	3.582	2.941
0.020	24.90	8.371	581.7646	5.180	3.521	53.71	3.589	2.959
0.025	23.15	8.386	586.5864	5.221	3.539	54.66	3.599	2.954
0.030	20.20	8.393	589.7454	5.230	3.542	56.06	3.605	2.953

The determined results of lattice constant (a) are recorded in Table-1 and Fig. 2 demonstrated the compositional variation of lattice constant (a) for the Ho concentration. The computed lattice constant values were found to be in the range 0.837 and 0.8393 nm. The variation of lattice constant (a) may be due to the replacement of Ho^{3+} (0.95 Å), more substantial ionic radii ions than Fe^{3+} (0.645 Å) ions at the octahedral site, resulting in a modest modification in the lattice constant [30]. Applying the constant lattice results and the unit cell volume (eqn. 3) of the Ho-doped Mg-Cu samples was computed [31]:
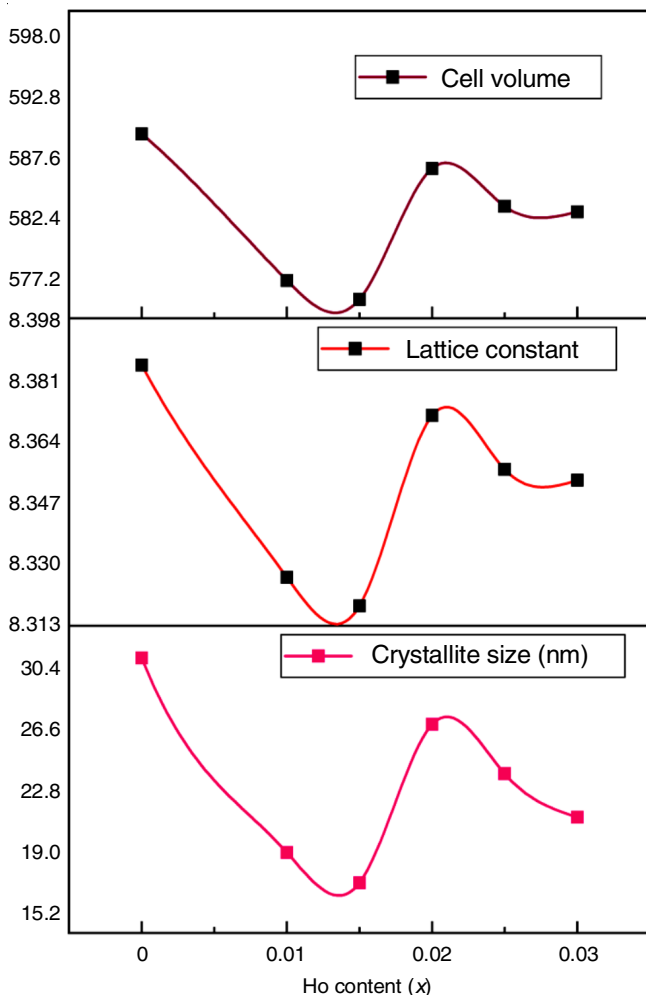
$$V = a^3 \tag{3}$$

Fig. 2. Plotted of Ho concentrations compared to crystalline size, lattice parameter and cell volume of Mg$_{0.5}$Cu$_{0.5}$Ho$_x$Fe$_{2-x}$O$_4$

The resultant unit cell volume exhibits a similar pattern to that of the lattice constant results, which are precisely proportional to the lattice constant (a). The values of the X-ray density (d$_x$) were calculated using eqn. 4, which incorporates the coordination number (Z) of cubic lattices, molecular weight (M) of the respective compositions, unit cell volume (V) and Avogadro's number (N$_A$ = 6.0238 × 10^{23}) [32].

$$d_x = \frac{8M}{N_A a^3} \tag{4}$$

Table-1 presents a summary of the X-ray density values obtained and illustrates the variations in the composition of these values. Due to the different ionic radii of Ho^{3+} (0.91 Å) and the ions of Fe (0.645Å), the densities increased. The considerable increase in the value of d$_x$ from 4.948 g cm^{-3} to 5.230 g cm^{-3} is due to the relative high atomic weight of Ho (150.36 amu) compared to iron (55.845 amu) [33]. Additionally, it can be observed that bulk density values are significantly lower than X-ray density values.

$$d_B = \frac{m}{\pi r^2 t} \tag{5}$$

where r = radius of circular pallet, t = width and m = mass (g). The bulk density of the synthesized Mg-Cu-Ho ferrite samples doped with rare earth elements was found to be increased. The average bulk density was between 2.732 g/cm^3 and 3.542 g/cm^3 with additional dopant content [34]. The porosity (P%) was also calculated using eqn. 5 [35,36]:

$$P\,(\%) = \left(1 - \frac{d_B}{d_x}\right) \times 100 \tag{6}$$

where d$_x$ is the X-ray density and d$_B$ is the bulk density of Ho^{3+} doped samples, the measured porosity was increased from 48.78 to 56.06%. The reduced porosity of the prepared samples may be due to compressive stress caused by the negative microstrain of lattice (Table-1). Moreover, the following relationships were used to calculate the hopping length (L$_A$ and L$_B$) and the values are shown in Table-1 [37]:

$$L_A = \frac{a\sqrt{3}}{4} \tag{7}$$

$$L_B = \frac{a\sqrt{2}}{4} \tag{8}$$

Morphological studies: The morphology and size of the samples have been examined using the field emission scanning electron microscope (FESEM).The FESEM and the EDS images of the synthesized $Mg_{0.5}Cu_{0.5}Ho_xFe_{2-x}O_4$ ($x = 0.00$-0.030) nanoferrites are shown in Figs. 3a-f and 4a-f, respectively. The grain size of the prepared nanoferrites varies between 50 and 63 nm and is in good alignment with the P-XRD crystallite size. Prepared Cu-Mg-Ho nanoferrites with sharp edges and spherical morphologies can be observed in the FESEM images [29]. The energy dispersive (EDS) spectra (Fig. 4a-f) revealed that in all the prepared nanoferrites ($x = 0.00$ to 0.030), only Cu, Mg, Ho, Fe and O are the main components. The quantitative analysis demonstrates that the chosen precursors were distributed uniformly following the desired composition.

The particle size distribution, agglomeration and lattice planes of the gprepared nanoferrites were also analyzed in detail using high-resolution transmission electron microscopy (HR-TEM). Fig. 5a-c shows the HR-TEM images of representative Mg-Cu-Ho ferrite with $x = 0.00$, 0.015 and 0.025, which is confirmed to be the cubic spinel structural of the desired composition. The Gauss fitting of the histogram revealed that the mean particle size of the prepared nanoferrites ranged from 41 to 53 nm is well arranged through the measured FESEM spectra. Fig. 6 shows the spectra of the selected area electron diffraction (SAED) of the nanoferrites $x = 0.00$, 0.015 and 0.025. By comparing the interplanar spacing calculated from the P-XRD analysis to that observed from the selected area

electron diffraction (SAED) images, it is evident that the diffraction rings observed correspond to the (440) plane. The presence of fringes at 0.245, 0.264, and 0.269 nm show that the spine nanoferrite formed a spinel cubic structure in the synthetic samples, as observed by (311) lattice planes.

FTIR studies: Fig. 7 shows the FTIR spectra of the prepared $Mg_{0.5}Cu_{0.5}Ho_xFe_{2-x}O_4$ ($x = 0.00$-0.030) nanoferrites recorded in the range from 4000-250 cm^{-1}. The stretching vibration of oxygen bonds produces these higher and lower peaks (Table-2), which show the development of spinel structure at the tetrahedral site in the range of 578-574 cm^{-1} may be due to the tetrahedral cluster stretching mode and the octahedral site in the range of 422-414 cm^{-1} [38,39]. The lower frequency band may be attributed to octahedral cluster stretching. The absence of frequency bands linked to other groups suggests that the nanoferrite samples were produced, as evidenced by the spectra, which exhibit its distinctive characteristics. However, the prep-

TABLE-2
ABSORPTION BAND AT A-SITE AND B-SITE FOR
$Mg_{0.5}Cu_{0.5}Ho_xFe_{2-x}O_4$ ($x = 0.00$ to 0.030) NANOFERRITES

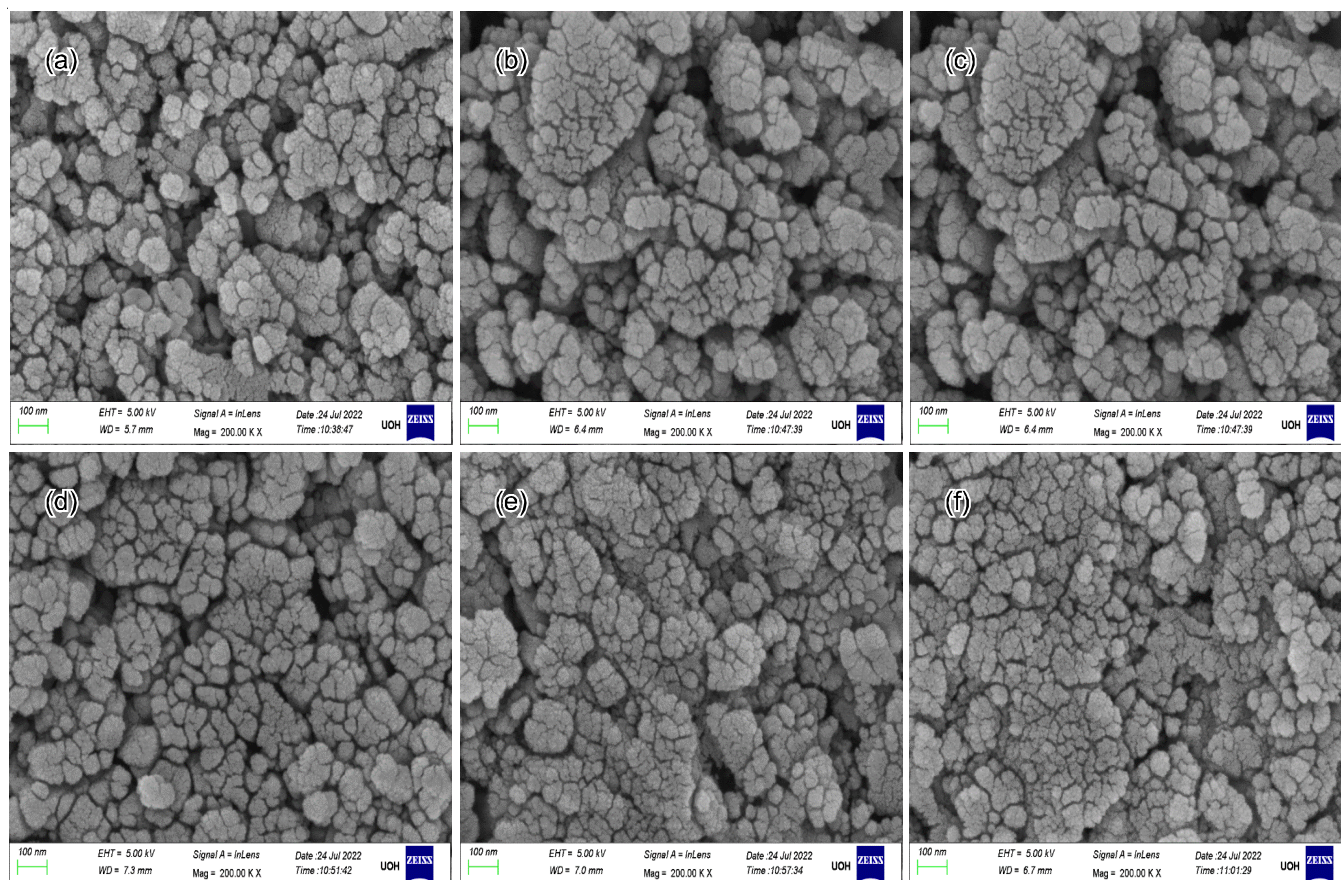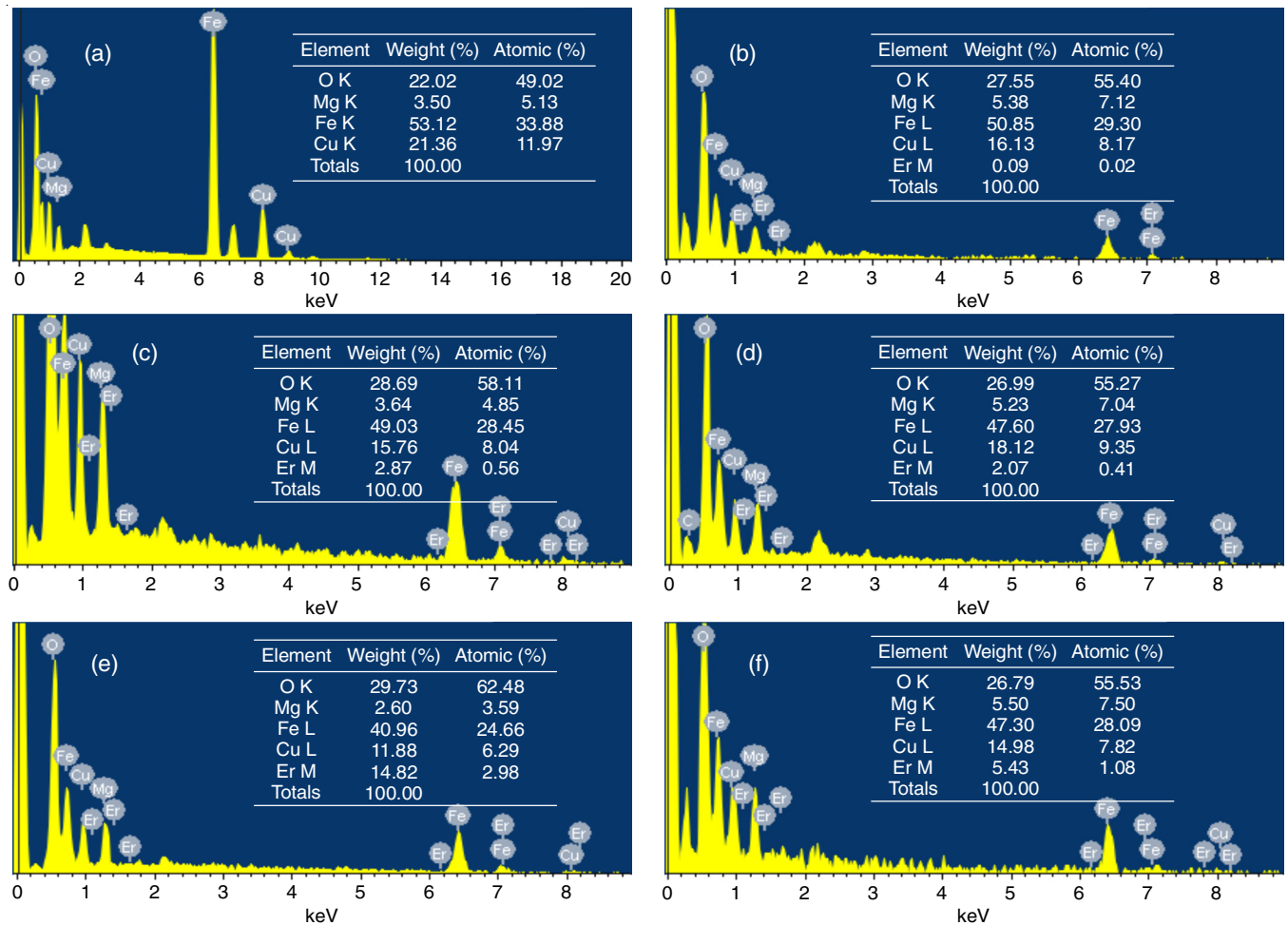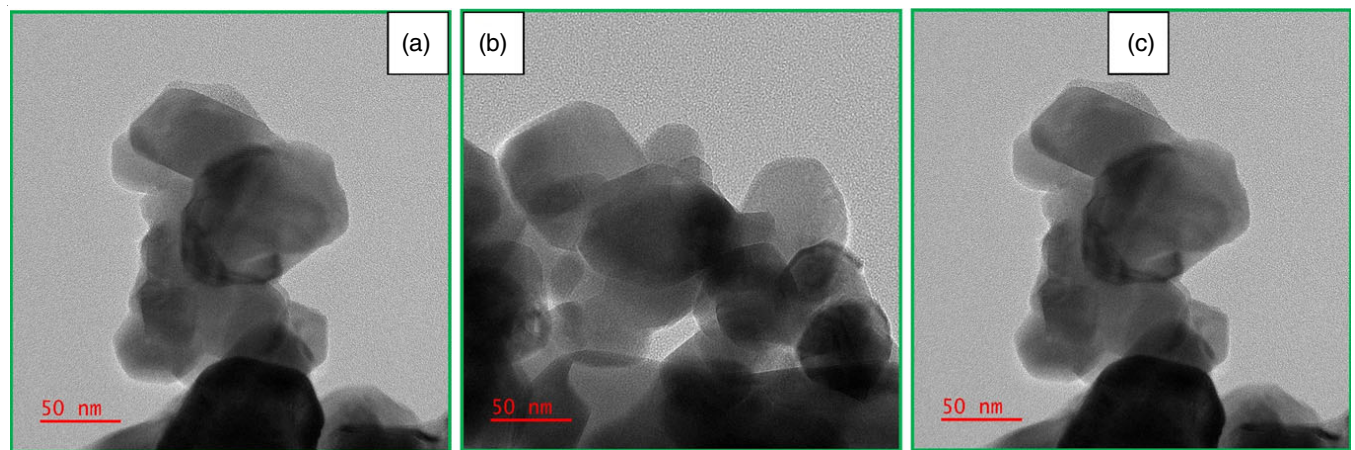| Samples (x)	High frequency (∂_1)	Low frequency (∂_2)
0.000	574.90	414.80
0.010	581.04	412.12
0.015	582.88	414.10
0.020	584.32	416.02
0.025	576.81	419.32
0.030	578.14	422.30

Fig. 3. FE-SEM images of $Mg_{0.5}Cu_{0.5}Ho_xFe_{2-x}O_4$ ($x = 0.00$ to 0.030) nanoferrite

(a)

Element	Weight (%)	Atomic (%)
O K	22.02	49.02
Mg K	3.50	5.13
Fe K	53.12	33.88
Cu K	21.36	11.97
Totals	100.00	

(b)

Element	Weight (%)	Atomic (%)
O K	27.55	55.40
Mg K	5.38	7.12
Fe L	50.85	29.30
Cu L	16.13	8.17
Er M	0.09	0.02
Totals	100.00	

(c)

Element	Weight (%)	Atomic (%)
O K	28.69	58.11
Mg K	3.64	4.85
Fe L	49.03	28.45
Cu L	15.76	8.04
Er M	2.87	0.56
Totals	100.00	

(d)

Element	Weight (%)	Atomic (%)
O K	26.99	55.27
Mg K	5.23	7.04
Fe L	47.60	27.93
Cu L	18.12	9.35
Er M	2.07	0.41
Totals	100.00	

(e)

Element	Weight (%)	Atomic (%)
O K	29.73	62.48
Mg K	2.60	3.59
Fe L	40.96	24.66
Cu L	11.88	6.29
Er M	14.82	2.98
Totals	100.00	

(f)

Element	Weight (%)	Atomic (%)
O K	26.79	55.53
Mg K	5.50	7.50
Fe L	47.30	28.09
Cu L	14.98	7.82
Er M	5.43	1.08
Totals	100.00	

Fig. 4. EDS images of Mg$_{0.5}$Cu$_{0.5}$Ho$_x$Fe$_{2-x}$O$_4$ (x = 0.00 to 0.030) nanoferrite

Fig. 5. HR-TEM images of Mg$_{0.5}$Cu$_{0.5}$Ho$_x$Fe$_{2-x}$O$_4$ (x = 0.00 to 0.030) nanoferrite

ared Ho-doped cubic spinel nanoferrite confirmed the successful development of the cubic phase. The observed band at 3420 cm⁻¹ is associated to with O-H vibration in the prepared spinel ferrite materials. In contrast, the absorption band in the 1546 cm⁻¹ is closely connected to ambient CO_2 gas. Additionally, the absorption band at 2340 cm⁻¹ is associated with the C-H group [40,41].

Absorption spectral studies: The optical properties of Ho-doped Mg-Cu (x = 0.00-0.030) nanoferrites recorded at the ambient temperature over the wavelength range of 200-650 nm were examined using a UV-visible spectrometer (Fig. 8). The Tauc's relation was used to calculate the optical band gap, which is influenced by the wavelength-dependent absorption:
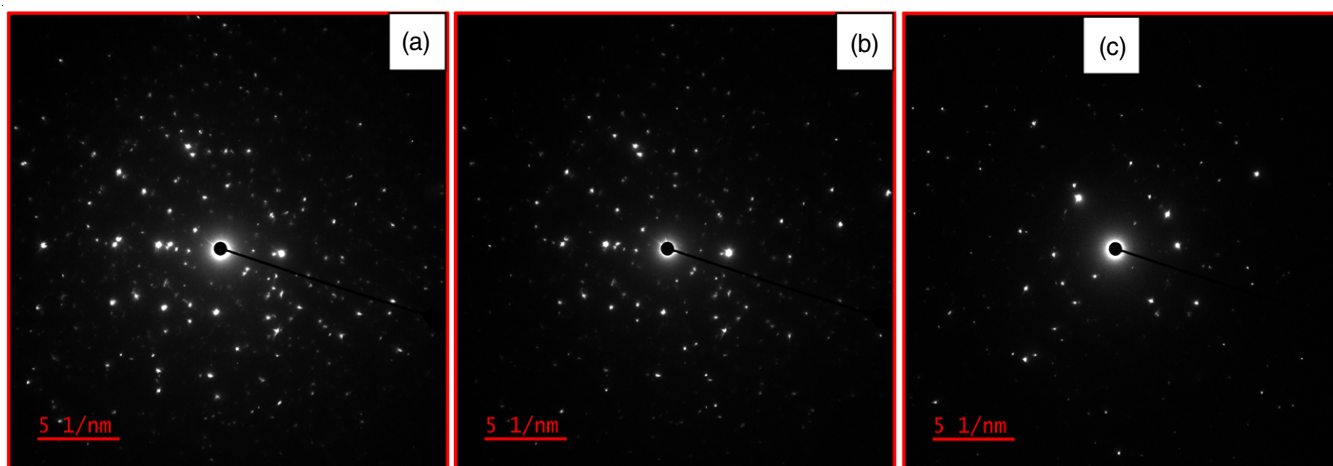
$$(\alpha n v)^n = A_x (h\alpha - E_g) \tag{8}$$

Fig. 6. SEAD images of $Mg_{0.5}Cu_{0.5}Ho_xFe_{2-x}O_4$ [x = (a) 0.00, (b) 0.010 and (c) 0.030] nanoferrite

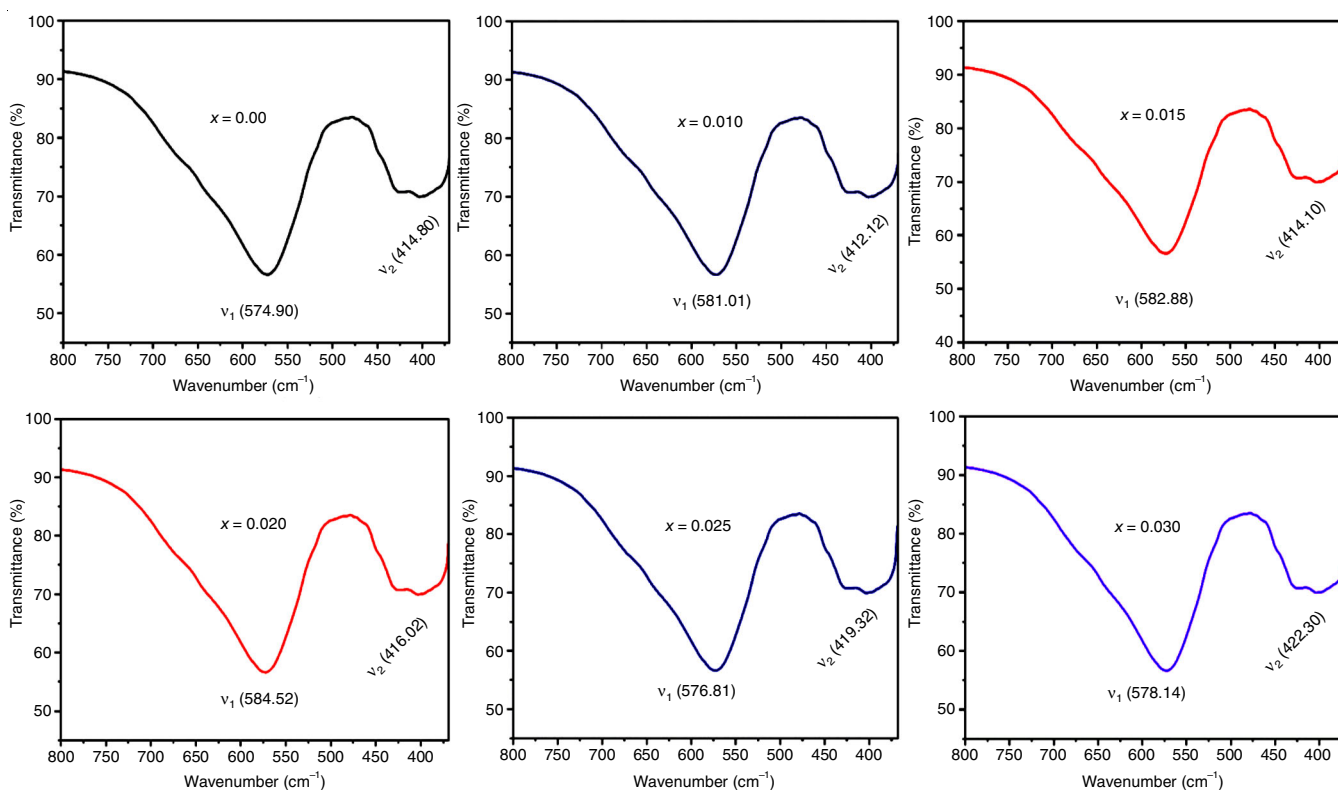Fig. 7. FTIR spectra of $Mg_{0.5}Cu_{0.5}Ho_xFe_{2-x}O_4$ (x = 0.00 to 0.030) nanoferrite

where α is the absorption coefficient, h is the plank constant (6.626×10^{-34} J s), ν is the photon energy (in eV), A is the proportionality constant, which depends on the probability of the transition and 'n' is a constant linked to the permitted direct or indirect transition probability [42]. According to reported work, spinel nanoferrites exhibit optical absorption spectra which are referred by direct electronic transitions. The optical band gap energy of the prepared materials is shown in Fig. 9. When external impurities are incorporated, semiconducting spinel ferrite usually changes the band gap. In this work, Ho^{3+} ions replace the B-site Fe^{3+} cations when the Ho^{3+} content is doped, which may lead to the formation of an impurity band inside the gap. Thus, the energy band gap (E_g) showed an increasing pattern and was determined to be 1.12-2.24 eV, as shown in Table-3. The reduction of Fe^{3+} to Fe^{2+} ions may be the reason for the energy band gap fluctuation [43].

TABLE-3
BAND GAP ENERGY VALUES (E_g) FOR
$Mg_{0.5}Cu_{0.5}Ho_xFe_{2-x}O_4$ (x = 0.00 to 0.030) NANOFERRITES

Samples (x)	Band gap (eV)
0.000	1.12
0.010	1.83
0.015	2.00
0.020	2.24
0.025	2.22
0.030	2.24

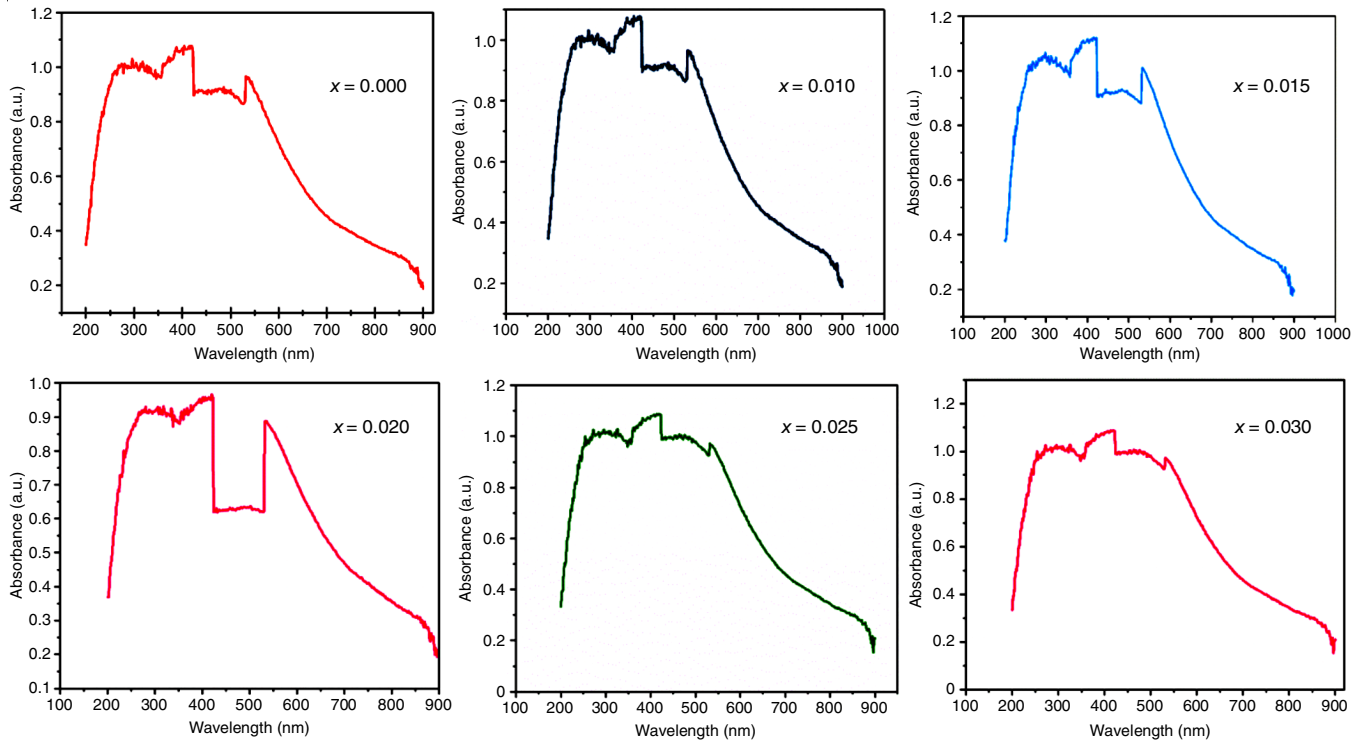Fig. 8. UV absorbance spectra of Mg$_{0.5}$Cu$_{0.5}$Ho$_x$Fe$_{2-x}$O$_4$ Mg$_{0.5}$Cu$_{0.5}$Ho$_x$Fe$_{2-x}$O$_4$ (x = 0.00 to 0.030) nanoferrite
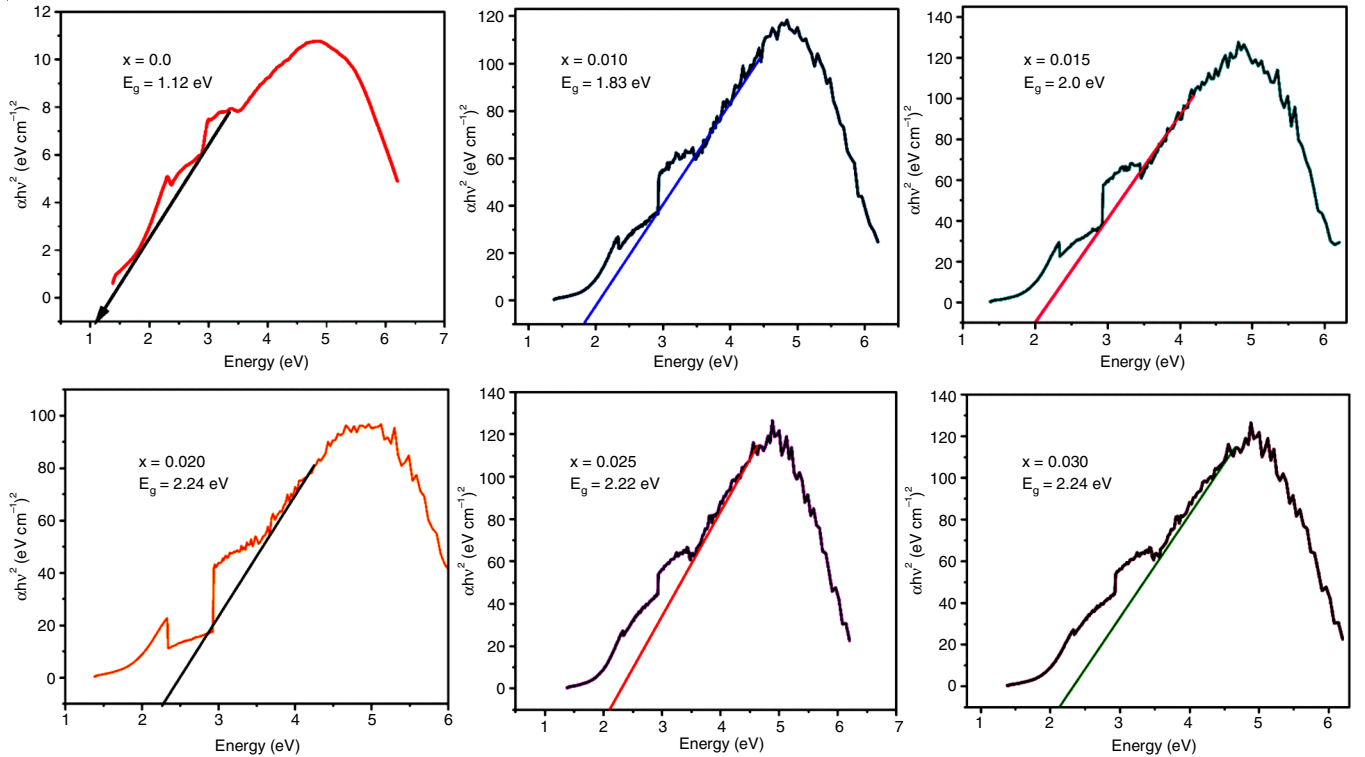
Fig. 9. Tauc plots to compute indirect energy band gap Mg$_{0.5}$Cu$_{0.5}$Ho$_x$Fe$_{2-x}$O$_4$ (x = 0.00 to 0.030) nanoferrite

I-V Measurement: Eqn. 12 is used to evaluate the properties of a certain material that impede the flow of electrical resistance [38,39]:

$$\rho = \frac{RA}{L} \qquad (12)$$

The shift in DC resistivity in the Ho³⁺ doped magnesium-copper nanoferrites (x = 0.00-0.030) is shown in Fig. 10. It is observed shows that DC resistivity rises from 5.837×10^6 to 4.105×10^7 as Ho³⁺ concentration rises, which is consistent with the Verway's hopping mechanism. The electric conduction in ferrous ions is primarily due to the movement of electrons
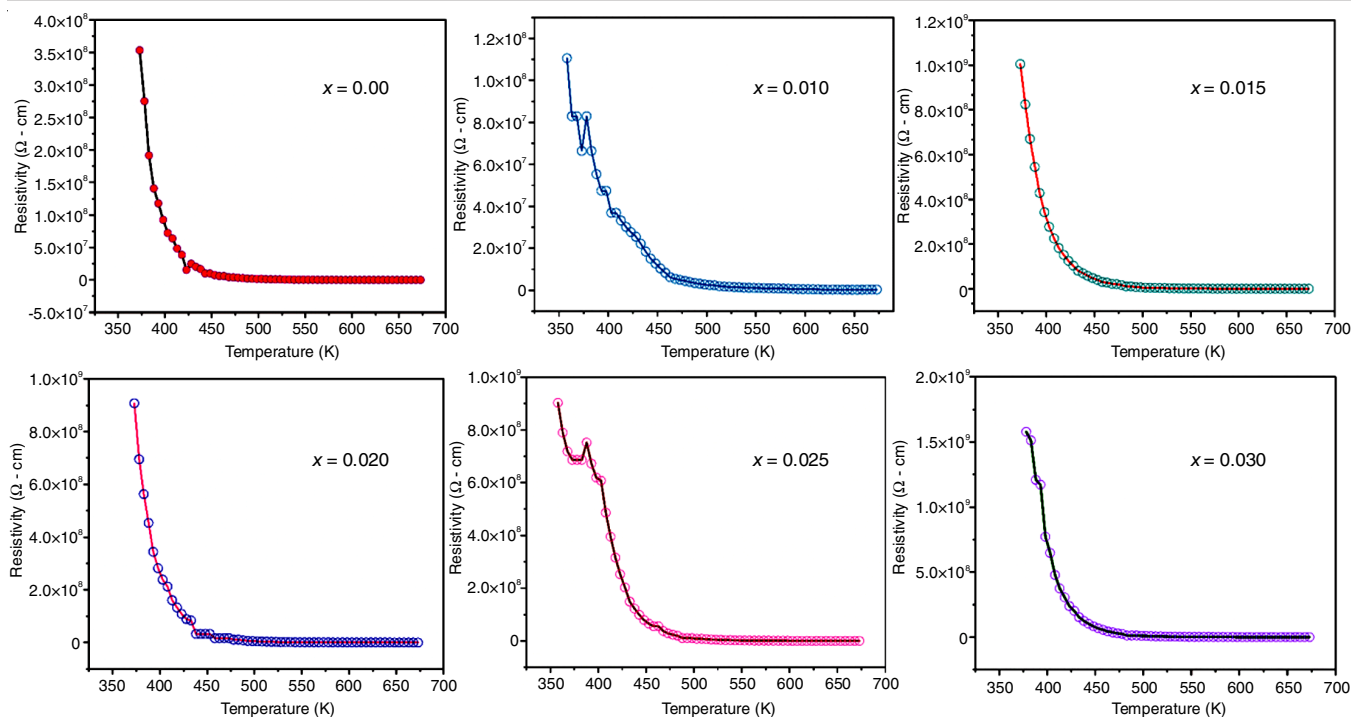
Fig. 10. Temperature-dependent dc resistivity of $Mg_{0.5}Cu_{0.5}Ho_xFe_{2-x}O_4$ (x = 0.00 to 0.030) nanoferrite

that are randomly distributed across the lattice sites, which are structurally comparable, and they move between ions of the same element that have different valence positions. Since the B-B sites are closer together than B-A sites, the possibility of electron jumping among B-A and B-B sites is much lower. Absence of Ho^{3+} inclusion (x = 0.00), Fe concentration is at its highest at the B-site and allows iron oxides to generate electricity. A reduction in the percentage of Cu and Mg ions is observed at B-site as the amount of Ho^{3+} in the A-site increases. As a result, some Fe^{3+} ions will move from the A site to the B site to make room for the extra Ho^{3+} ions at the A sites. As a result, at B-site, there is more electron hopping between Fe^{2+} and Fe^{3+}. A decrease in the conduction caused by Fe^{2+} ion is followed by a rise in resistance. Additionally, the microstructural elements like grain size, pores and grain boundaries have an impact on DC resistivity. The relationship between resistivity and the size of grains revealed suggests that resistivity is inversely related to the grain size. Therefore, it is anticipated that the resistivity of Cu-Mg ferrite will increase as Ho content rises.

Based on the Arrhenius relation, the curve relating log and 1000/T for samples with x = 0.00 to 0.030 is shown in

Fig. 11. There is a difference in the slope of the graph in a few nanoferrite samples, which indicates that there are two independent conducting processes that have different activation energies. In the majority of nanoferrites, a straight line with a slope equivalent to activation energy can be observed throughout a broad temperature range. It is due to the fact that the Curie temperature (T_C) of the prepared nanoferrites exceeds the present range of recorded temperatures, the application of the least square fit approach in this study to create straight lines did not produce a line that remained straight beyond the Curie temperature. This slope modification often takes place at temperatures close to the Curie temperatures of the samples. From the linear plots (Fig. 11) of resistivity, the activation energy of each sample within the temperature range of 0.3649-0.2493 eV can be calculated and the results are shown in Table-4.

Thermoelectric power (TEP) analysis: Fig. 12 depicts the fluctuation of Seebeck coefficient with temperature for the $Mg_{0.5}Cu_{0.5}Ho_xFe_{2-x}O_4$ nanoferrites (x = 0.00, 0.01, 0.015, 0.02, 0.025 and 0.030). At normal temperature, all ferrites except with x = 0.025 composition show a positive Seebeck coefficient,

TABLE-4
ACTIVATION ENERGY IN THE FERROMAGNETIC REGION (E_P), PARAMAGNETIC REGION (E_F), CURIE (T_C),
TEMPERATURE (T_C) AND RESISTIVITY (ρ) FOR $Mg_{0.5}Cu_{0.5}Ho_xFe_{2-x}O_4$ (x = 0.00 to 0.030) NANOFERRITES

Content (*x*)	Activation energies		ΔE (eV)	T_S (K) resistivity	Resistivity	
	E_P (eV)	E_F (eV)			at T_C K	at 673 K
0.000	0.4216	0.0567	0.3649	458	5.837×10^6	2.225×10^4
0.010	0.3860	0.0699	0.3161	475	5.452×10^5	3.137×10^5
0.015	0.3664	0.0716	0.2948	481	3.166×10^7	6.877×10^4
0.020	0.3568	0.0891	0.2677	486	3.575×10^7	6.989×10^4
0.025	0.3329	0.0778	0.2551	491	3.920×10^7	7.890×10^4
0.030	0.3178	0.0685	0.2493	498	4.105×10^7	8.567×10^4
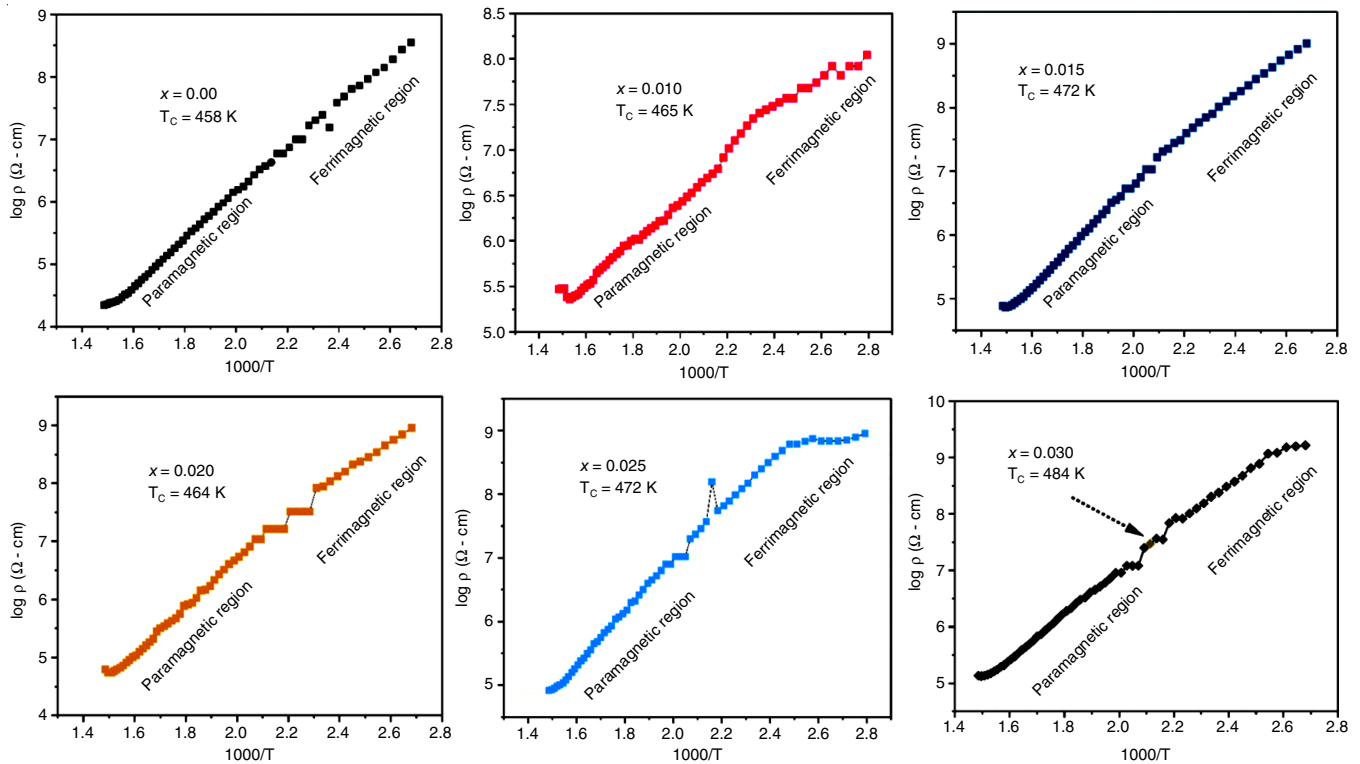
Fig. 11. Plots of 1000/T *vs.* log row of Mg$_{0.5}$Cu$_{0.5}$Ho$_x$Fe$_{2-x}$O$_4$ (x = 0.00 to 0.030) nanoferrite
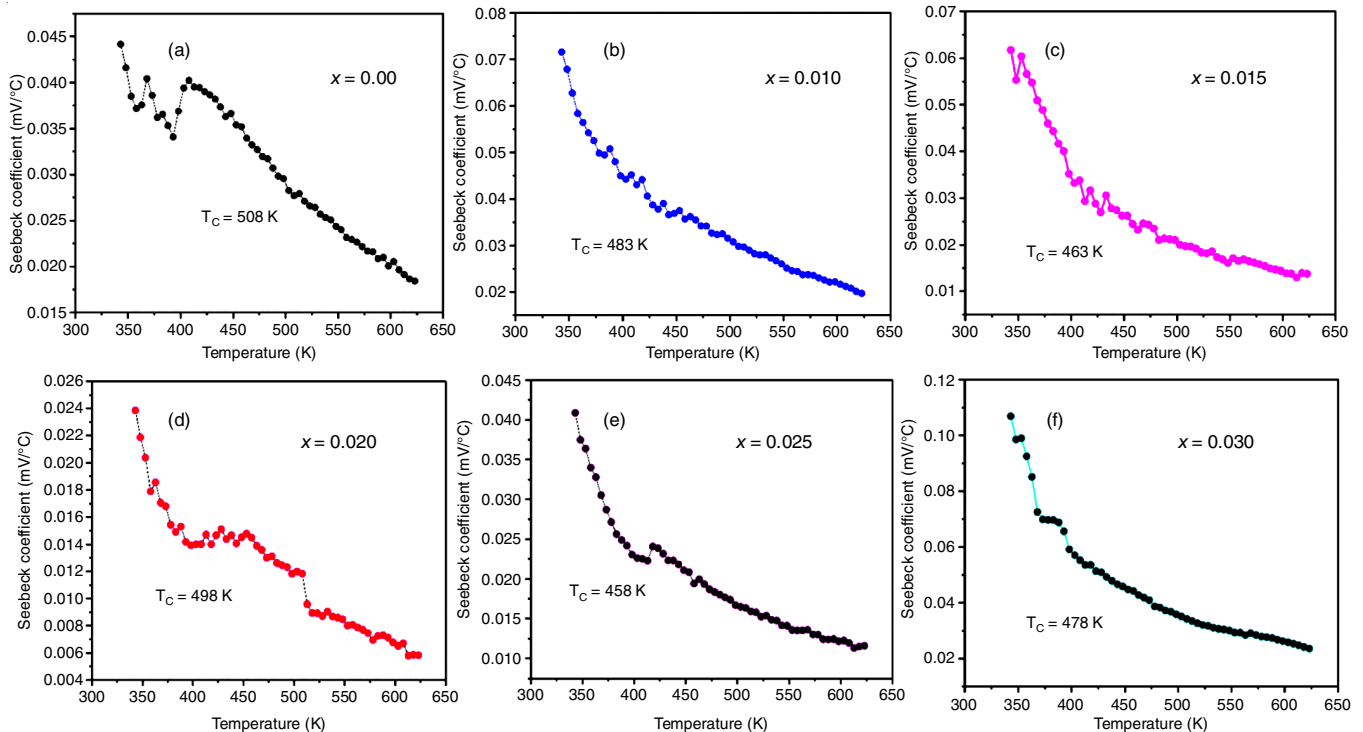
Fig. 12. Difference of Seebeck coefficient with temperature Mg$_{0.5}$Cu$_{0.5}$Ho$_x$Fe$_{2-x}$O$_4$ (x = 0.00 to 0.030) nanoferrite

indicating that they are all p-type semiconducting materials. The Seebeck coefficient of pure Mg-Cu nanoferrite shows positive values between 55 ℃-110 ℃, 185 ℃-310 ℃ and 340 ℃-410 ℃, indicating the p-type behaviour, while it turns negative between 90 ℃-165 ℃ and 290 ℃-350 ℃, indicating n-type behaviour (Fig. 12a). The Seebeck value for all Ho-doped

Mg-Cu nanoferrites becomes positive between 40 ℃ and 230 ℃, suggesting p-type semiconducting behaviour, while it becomes negative between 250 ℃-400 ℃, indicating n-type behaviour (Fig. 12b-f). The p-type semiconducting behaviour of the nanoferrites under study can be explained by the availability of the additional vacancies caused by the presence of Mg²⁺

ions on the octahedral site instead of Fe^{3+} ions in the prepared $Mg_{0.5}Cu_{0.8}Ho_xFe_{2-x}O_4$ nanoferrites. Due to the lower charge of Cu^{2+} ions compared to Fe^{3+}, the excess vacancies which arise from this would be oxygen vacancies rather than the cation vacancies. With increasing Mg^{2+} occupancy, these oxygen vacancies grow, resulting in a positive Seebeck coefficient (Table-5). The Seebeck coefficient may have decreased due to a decrease in the oxygen vacancies. The hopping of electrons from Fe^{2+} to Fe^{3+} ions is thought to be the cause of the n-type semiconducting behaviour.

Fig. 13. Magnetic hysteresis loop of $Mg_{0.5}Cu_{0.5}Ho_xFe_{2-x}O_4$ ($x = 0.00$ to 0.030) nanoferrite

TABLE-5
CURIE (T_C), TEMPERATURE (T_C) AND SEEBECK COEFFICIENT FOR $Mg_{0.5}Cu_{0.5}Ho_xFe_{2-x}O_4$ ($x = 0.00$ to 0.030) NANOFERRITES

Content (x)	Seebeck -T_C	Seebeck coefficient
0.000	493	4023
0.010	488	3565
0.015	478	3298
0.020	468	3134
0.025	478	2489
0.030	466	2445

Magnetic analysis: Fig. 13 shows that the M-H loops of the Ho-doped Mg-Cu ferrites ($x = 0.00$-0.030) were calculated by the VSM method at room temperature (300 K). The hysteresis loops showing ferromagnetic behaviour indicate the saturation in magnetization at the high value of 20 Oe of the applied field. The magnetic parameters determined from M-H hysteresis loops of the ferrites include saturation magnetization (M_s), coercivity (H_c), retentivity (M_r), magnetic moment (μ_B), squareness ratio (SQR), anisotropy constant (K) initial permeability (μ_i). The obtained values are recorded in Table-6. The S-shape with no opening cycles is shown by the Ho-doped Mg-Cu all prepared sample M-H loos (*i.e.* low vales retentivity and small vales coercivity). At 300 K (room temperature), this behaviour corresponds to the superparamagnetic behaviour of the prepared nanoferrites smaller than 45 nm. Nanoparticle spinel ferrites exhibited primarily superparamagnetic behaviour. The P-XRD observations above demonstrated a crystallite size of less than 42 nm. The saturation magnetization decreases and the resulting saturation (M_s) ranges between 6.85-4.65 emu/g. The decreasing M_s values depended on several factors like crystalline size, surface spin effects, cation distribution and the M_s values, which contribute the favourable super-paramagnetic behaviour [44,45]. The nanoferrite samples with $x = 0.00$ have the highest coercivity (H_c) value of 340.12 Oe and also exhibits the lowest M_s value of 30.55 emu/g. Thus, the reported values of $Ho^{3+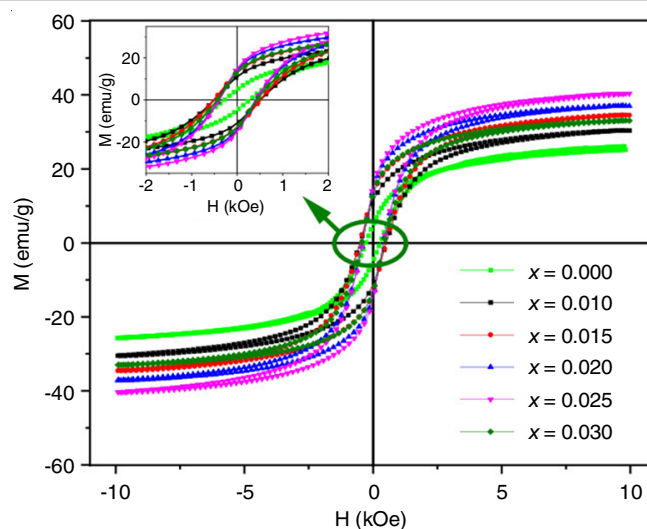}$ doped Mg-Cu nanoferrites indicate that the samples have a soft nature. Furthermore, the lowered H_c value indicates a reduction in the magneto-crystalline anisotropy. As the Holonium concentration in the samples increased, it was also observed that the remanence magnetization reduces from 16.25 to 10.88 emu/g. The Ho doped nanoferrites had the lowest remanent magnetization value suggesting that the sample exhibits increased superparamagnetic-like behaviour due to the low doping content of Ho^{3+} ions. The lower proportion of remanent or squareness (SQR) ratio indicates the isotropic nature of the materials. The more significant proportion indicates that magnetization directions have been reoriented to the closest axis. The squareness ratio of the prepared samples in the current study ranges between 0.53 and 0.57, indicating no significant change [46].

Furthermore, the initial permeability (K) and anisotropy constant (μ_i) of Ho^{3+}-doped Mg-Cu nanoferrites were also determined using eqns. 12 and 13 and the results are listed in Table-6.

$$K = \frac{M_s \times H_c}{0.96} \quad (9)$$

$$\mu_i = \frac{M_s^2 \times D}{K} \quad (10)$$

Conclusion

The citric sol-gel auto-combustion process has successfully produced Ho^{3+} substituted $Mg_{0.5}Cu_{0.5}Ho_xFe_{2-x}O_4$ ferrite systems ($x = 0.000, 0.005, 0.010, 0.015, 0.020, 0.025$ and 0.030). The Mg-Cu ferrite matrix is replaced with holonium

TABLE-6
MAGNETIC PARAMETERS VALUES OF $Mg_{0.5}Cu_{0.5}Ho_xFe_{2-x}O_4$ ($x = 0.00$ to 0.030) NANOFERRITES

Samples	Saturation magnetization	Coercive field	Remnant magnetization	SQR	Anisotropy constant	Initial permeability
0.000	30.55	340.12	16.25	0.53	10823.610	29893.679
0.010	28.56	321.11	16.10	0.56	9553.022	18393.439
0.015	26.21	280.55	15.51	0.59	7659.599	11747.086
0.020	24.13	276.87	14.17	0.58	6959.242	14498.196
0.025	20.55	255.60	12.11	0.58	5471.437	9776.3028
0.030	18.88	200.15	10.88	0.57	3936.283	7200.3780

ions, which results in the development of a single cubic spinel ferrite structure and an increase in lattice constant. The FESEM, HRTEM, EDX and SEAD were employed to reveal the cubic morphology and chemical compositions. The crystallite size ranged from 17.10-32.03 nm and the lattice constant was 8.408-8.356. The most intense peak in the XRD spectra was reported at $2\theta = 35°$ which indicate the formation of an FCC spinel structure. FTIR studies exhibited two substantial peaks in 400 562-400 cm^{-1} region showing the metal-oxygen stretching and the formation of synthesized ferrite materials. The band gap energies were varied from 3.010 to 3.297 eV as assigned from the UV-vis spectral analysis. At ambient temperature, the saturation magnetization, coercively and remanent magnetization from M-H loops were lowered when Ho^{3+} was doped in Mg-Cu ferrites. The M-H loop analyses showed the super-paramagnetic behaviour of the prepared nanoferrites. The M-H curve demonstrates that M_S initially decreases to 16.25 from 10.88 emu/g with a decrease in doping concentration. This phenomenon is brought on by an A-B type super-exchange contact in the synthesized nanoferrites. The fluctuations in the coercivity (H_c) and magnetic anisotropy (K_1) indicate the thermal stability of all the samples regarding applications and could be applied to solenoids and transformers.

CONFLICT OF INTEREST

The authors declare that there is no conflict of interests regarding the publication of this article.

REFERENCES

1. N. Sanpo, C.C. Berndt, C. Wen and J. Wang, *Acta Biomater.*, **9**, 5830 (2013);
https://doi.org/10.1016/j.actbio.2012.10.037

2. S.E. Shirsath, R.H. Kadam, A.S. Gaikwad, A. Ghasemi and A. Morisako, *J. Magn. Magn. Mater.*, **323**, 3104 (2011);
https://doi.org/10.1016/j.jmmm.2011.06.065

3. S. Abbas, M. Fatima-Tuz-Zahra and M. Anis-ur-Rehman, *J. Alloys Compd.*, **677**, 143 (2016);
https://doi.org/10.1016/j.jallcom.2016.03.148

4. L.Z. Li, Z. Yu, Z.W. Lan, K. Sun and C.J. Wu, *Ceram. Int.*, **40**, 13917 (2014);
https://doi.org/10.1016/j.ceramint.2014.05.112

5. M.N. Akhtar, M.A. Khan, M.R. Raza, M. Ahmad, G. Murtaza, R. Raza, S.F. Shaukat, M.H. Asif, M. Saleem and M.S. Nazir, *Ceram. Int.*, **40**, 15821 (2014);
https://doi.org/10.1016/j.ceramint.2014.07.109

6. R. Ali, A. Mahmood, M.A. Khan, A.H. Chughtai, M. Shahid, I. Shakir and M.F. Warsi, *J. Alloys Compd.*, **584**, 363 (2014);
https://doi.org/10.1016/j.jallcom.2013.08.114

7. L. Wang, H.B. Li, J. Li, M. Liu, Y.M. Zhang, *Hyperfine Interactions*, **222**, 37 (2012);
https://doi.org/10.1007/s10751-012-0633-4

8. Z. Bitar, D. El-Said Bakeer and R. Awad, *Turk. J. Phys.*, **43**, 80 (2019);
https://doi.org/10.3906/fiz-1808-22

9. R.S. Melo, F.C. Silva, K.R.M. Moura, A.S. de Menezes and F.S.M. Sinfrônio, *J. Magn. Magn. Mater.*, **381**, 109 (2015);
https://doi.org/10.1016/j.jmmm.2014.12.040

10. Y. Liu, J.J. Li, F.F. Min, J.B. Zhu and M.X. Zhang, *J. Magn. Magn. Mater.*, **354**, 295 (2014);
https://doi.org/10.1016/j.jmmm.2013.11.005

11. R.K. Mudsainiyan, S.K. Chawla and S.S. Meena, *J. Alloys Comp.*, **615**, 875 (2014);
https://doi.org/10.1016/j.jallcom.2014.07.035

12. P. Punia, P. Thakur, R. Kumar, R. Syal, R. Dhar and A. Thakur, *J. Alloys Comp.*, **928**, 167248 (2022);
https://doi.org/10.1016/j.jallcom.2022.167248

13. I.H. Lone, J. Aslam, N.R.E. Radwan, A. Akhter, A.H. Bashal and R.A. Shiekh, *Curr. Anal. Chem.*, **16**, 826 (2020);
https://doi.org/10.2174/1573411015666191203102837

14. A. Anupama, V. Kumaran and B. Sahoo, *Adv. Powder Technol.*, **29**, 2188 (2018);
https://doi.org/10.1016/j.apt.2018.06.002

15. H. Fakhr Nabavi, M. Aliofkhazraei, M. Hasanpoor and A. Seyfoori, *Int. J. Appl. Ceram. Technol.*, **13**, 1112 (2016);
https://doi.org/10.1111/ijac.12580

16. A. Gholizadeh, *J. Am. Ceram. Soc.*, **100**, 3577 (2017);
https://doi.org/10.1111/jace.14896

17. N. Shamgani and A. Gholizadeh, *Ceram. Int.*, **45**, 239 (2019);
https://doi.org/10.1016/j.ceramint.2018.09.158

18. A. Gholizadeh, *J. Mater. Res. Technol.*, **8**, 457 (2019);
https://doi.org/10.1016/j.jmrt.2017.12.006

19. A. Balamurugan, R. Shunmuga Priya, P Chaudhary, E.R. Kumar, T. Indumathi, Ch Srinivas, B.C. Yadav and D.L. Sastry, *Ceram. Int.*, **48**, 4874 (2022);
https://doi.org/10.1016/j.ceramint.2021.11.024

20. J. Li, X. Wang, K. Song, Q. Li, R. Gong, Z. Su, Y. Chen and V.G. Harris, *IEEE Trans. Magnet.*, **51**, 1 (2015);
https://doi.org/10.1109/tmag.2015.2428718

21. O. Mounkachi, M. Hamedoun, M. Belaiche, A. Benyoussef, R. Masrour, H. El Moussaoui and M. Sajieddine, *Physica B*, **407**, 27 (2012);
https://doi.org/10.1016/j.physb.2011.09.023

22. M. Selvakumar, S. Maruthamuthu, E. Vijayakumar, B. Saravanakumar and A.T. Dhiwahar, *J. Electron. Mater.* (2024);
https://doi.org/10.1007/s11664-024-11293-5

23. M. Kamran and M. Anis-ur-Rehman, *Ceram. Int.*, **48**, 16912 (2022);
https://doi.org/10.1016/j.ceramint.2022.02.246

24. S.I. Ahmad, *J. Magn. Magn. Mater.*, **562**, 169840 (2022);
https://doi.org/10.1016/j.jmmm.2022.169840

25. M. Hashim, M. Raghasudha, S.S. Meena, J. Shah, S.E. Shirsath, S. Kumar, D. Ravinder, P. Bhatt, R. Alimuddin, R. Kumar and R.K. Kotnala, *J. Magn. Magn. Mater.*, **449**, 319 (2018);
https://doi.org/10.1016/j.jmmm.2017.10.023

26. M. Khairy, W.A. Bayoumy, S.S. Selima and M.A. Mousa, *J. Mater. Res.*, **35**, 2652 (2020);
https://doi.org/10.1557/jmr.2020.200

27. P. Imanipour, S. Hasani, M. Afshari, S. Sheykh, A. Seifoddini and K. Jahanbani-Ardakani, *J. Magn. Magn. Mater.*, **510**, 166941 (2020);
https://doi.org/10.1016/j.jmmm.2020.166941

28. F. Sharifianjazi, M. Moradi, N. Parvin, A. Nemati, A. Jafari Rad, N. Sheysi, A. Abouchenari, A. Mohammadi, S. Karbasi, Z. Ahmadi, A. Esmaeilkhanian, M. Irani, A. Pakseresht, S. Sahmani and M.S. Asl, *Ceram. Int.*, **46**, 18391 (2020);
https://doi.org/10.1016/j.ceramint.2020.04.202

29. A. Hssaini, M. Belaiche, M. Elansary, C.A. Ferdi and Y. Mouhib, *J. Supercond. Nov. Magn.*, **35**, 2799 (2022);
https://doi.org/10.1007/s10948-022-06307-4

30. H. Nikmanesh, E. Jaberolansar, P. Kameli, A. Ghotbi Varzaneh, M. Mehrabi, M. Shamsodini, M. Rostami, I. Orue and V. Chernenko, *J. Magn. Magn. Mater.*, **543**, 168664 (2022);
https://doi.org/10.1016/j.jmmm.2021.168664

31. N. Amin, A. Razaq, A.U. Rehman, K. Hussain, M.A.U. Nabi, N.A. Morley, M. Amami, A. Bibi, M.I. Arshad, K. Mahmood, M. Fatima, M. Akhtar, S. Akbar, A. Manzoor, H.T. Ali, M. Yusuf and S. Amin, *J. Supercond. Nov. Magn.*, **34**, 2945 (2021);
https://doi.org/10.1007/s10948-021-06053-z

32. M.K. Bharti, S. Chalia, P. Thakur and A. Thakur, *J. Supercond. Nov. Magn.*, **34**, 2591 (2021);
https://doi.org/10.1007/s10948-021-05908-9

33. A. Munir, F. Ahmed, M. Saqib and M. Anis-ur-Rehman, *J. Supercond. Nov. Magn.*, **28**, 983 (2015);
https://doi.org/10.1007/s10948-014-2737-3

34. P. Punia, R. Dhar, B. Ravelo, A. Trukhanov, L. Panina, P. Thakur and A. Thakur, *J. Supercond. Nov. Magn.*, **34**, 2131 (2021);
https://doi.org/10.1007/s10948-021-05967-y

35. S. Ikram, J. Jacob, M.I. Arshad, K. Mahmood, A. Ali, N. Sabir, N. Amin and S. Hussain, *Ceram. Int.*, **45**, 3563 (2019);
https://doi.org/10.1016/j.ceramint.2018.11.015

36. S. Taneja, P. Thakur, B. Ravelo and A. Thakur, *Mater. Res. Bull.*, **154**, 111937 (2022);
https://doi.org/10.1016/j.materresbull.2022.111937

37. M.P. Ghosh, T.V. Muley, S. Roy, S. Mohanty and S. Mukherjee, *J. Supercond. Nov. Magn.*, **34**, 2643 (2021);
https://doi.org/10.1007/s10948-021-05944-5

38. V. Rathod, A. Anupama, R.V. Kumar, V.M. Jali and B. Sahoo, *Vib. Spectrosc.*, **92**, 267 (2017);
https://doi.org/10.1016/j.vibspec.2017.08.008

39. H. Javed, F. Iqbal, P.O. Agboola, M.A. Khan, M.F. Warsi and I. Shakir, *Ceram. Int.*, **45**, 11125 (2019);
https://doi.org/10.1016/j.ceramint.2019.02.176

40. B.P. Jacob, S. Thankachan, S. Xavier and E.M. Mohammed, *Phys. Scr.*, **84**, 045702 (2011);
https://doi.org/10.1088/0031-8949/84/04/045702

41. A. Riaz, M.A. Khan, M. Junaid, S. Gulbadan, A. Manzoor, S.R. Ejaz, G.A. Ashraf, H.H. Somaily, M. Morsi and T. Alshahrani, *Mater. Chem. Phys.*, **290**, 126519 (2022);
https://doi.org/10.1016/j.matchemphys.2022.126519

42. S.P. Keerthana, R. Yuvakkumar, P.S. Kumar, G. Ravi and D. Velauthapillai, *Environ. Res.*, **197**, 111047 (2021);
https://doi.org/10.1016/j.envres.2021.111047

43. A. Manohar, C. Krishnamoorthi, K.C.B. Naidu and C. Pavithra, *Appl. Phys., A Mater. Sci. Process.*, **125**, 477 (2019);
https://doi.org/10.1007/s00339-019-2760-0

44. H. Rao Daruvuri, K. Chandu, N. Murali, D. Parajuli, Y. Mulushoa S and M.P. Dasari, *Inorg. Chem. Commun.*, **143**, 109794 (2022);
https://doi.org/10.1016/j.inoche.2022.109794

45. P. Samoila, L. Sacarescu, A.I. Borhan, D. Timpu, M. Grigoras, N. Lupu, M. Zaltariov and V. Harabagiu, *J. Magn. Magn. Mater.*, **378**, 92 (2015);
https://doi.org/10.1016/j.jmmm.2014.10.174

46. P.P. Naik, S.S. Hasolkar, M.M. Kothawale and S.H.P. Keluskar, *Physica B*, **584**, 412111 (2020);
https://doi.org/10.1016/j.physb.2020.412111